PHYSICAL REVIEW APPLIED **22,** 014018 (2024)

Ultimate performance of microwave tissue ablation

Sangbin Lee,[1,2] Jongheon Lee,[3] Ada S.Y. Poon,[4] and Sanghoek Kim[1,2,*,†]
[1] *Department of Electronics and Information Convergence Engineering, Kyung Hee University, Yongin 17104, Republic of Korea*
[2] *Institute for Wearable Convergence Electronics, Kyung Hee University, Yongin 17104, Republic of Korea*
[3] *Ming Hsieh Department of Electrical Engineering, University of Southern California, California 90089, USA*
[4] *Department of Electrical Engineering, Stanford University, California 94305, USA*

(Received 8 March 2024; revised 9 June 2024; accepted 11 June 2024; published 9 July 2024)

Microwave ablation is a therapeutic procedure to eliminate abnormal tissue within a body selectively. There are two types of ablation; thermal ablation aims to raise the temperature at the target, while nonthermal ablation induces a temporarily high electric field at the target to disrupt cellular membrane integrity. This work identifies the fundamental bounds of the efficiency for each type of ablation and the sources to achieve them. For both types, the bounds exceed the performance of existing solutions tenfold, showing large room for improvement. Finally, the optimal source for thermal ablation is physically realized with an 11 × 11 dipole array, the performance of which closely approaches the bound.

DOI: 10.1103/PhysRevApplied.22.014018

I. INTRODUCTION

Focusing the field in a confined region has been a long-sought-after goal in both microwave [1,2] and optical [3,4] spectrums due to its various applications, such as high-resolution microscopes [4], lithography [5], biomedicines [6–8], and wireless-power-transfer systems [9,10]. Among them, microwave ablation for biomedical applications is different from the other applications: (1) the human tissue in which the wave travels is a lossy medium and (2) the depth of the target can be comparable to the source size, which is limited by the body scale. These distinctive features make focusing methods for other applications not directly applicable to biomedical ablation.

Biomedical ablation can be categorized into two types according to their purpose. The first type is *thermal ablation*, also known as "hyperthermia," which concentrates the field *spatially* at a target area for nearly 1 h to gradually increase the temperature of the target to 40–43 °C, so that apoptotic and necrotic cell death may occur in the target area [11] or make the cells more vulnerable to radiotherapy [12] or chemotherapy [13]. While it lacks a temporal focusing [Fig. 1(a), top], it tries to increase the temperature of a target sufficiently high [Fig. 1(b), top] after the operation.

The other type is *nonthermal ablation*, of which the purpose is to induce a high electric field momentarily at a target, leading to a sudden disruption of cell homeostasis [14], for which the *spatiotemporal* focusing of the field is necessary. It aims to induce spatiotemporal focusing of the electric field at a target [Fig. 1(a), bottom]. However, because the duration of the high electric field is very short, the temperature rise after the operation is not considerable [Fig. 1(b), bottom].

Over decades, various kinds of ablation applicator have been developed. Although the applicator with a single source could successfully destroy a superficial target, it is incapable of localizing the heat at deep tissue [15,16]. In an effort to deepen the target point, a coherent array of sources placed around the surface of tissue was proposed [Fig. 1(c)]. In the work reported in Refs. [17,18] the magnitude and phase of each source were optimized with use of the time-reversal method, in which the electric field at the target from each source should interfere in phase. For ablation, however, it is more directly associated with its purpose to optimize the *focusing gain*, which is defined as the ratio of the electric field strength at the target to the average electric field strength across the body. For example, in the work reported in Refs. [19–21], the source excitation to maximize the gain of time-averaged strength for thermal ablation was deduced.

In previous work, however, the sources were restricted to an array of discrete elements [Fig. 1(c)] with a specific type, such as horn [17], dipole antenna [19–21], or electric current filaments [22,23], which prevents the results from being the global optimum. Since any physical antenna has an inherent dependency on frequency, the optimal frequency obtained over a confined source

---

[*] Contact author: sanghoek@khu.ac.kr
[†] http://ael.khu.ac.kr

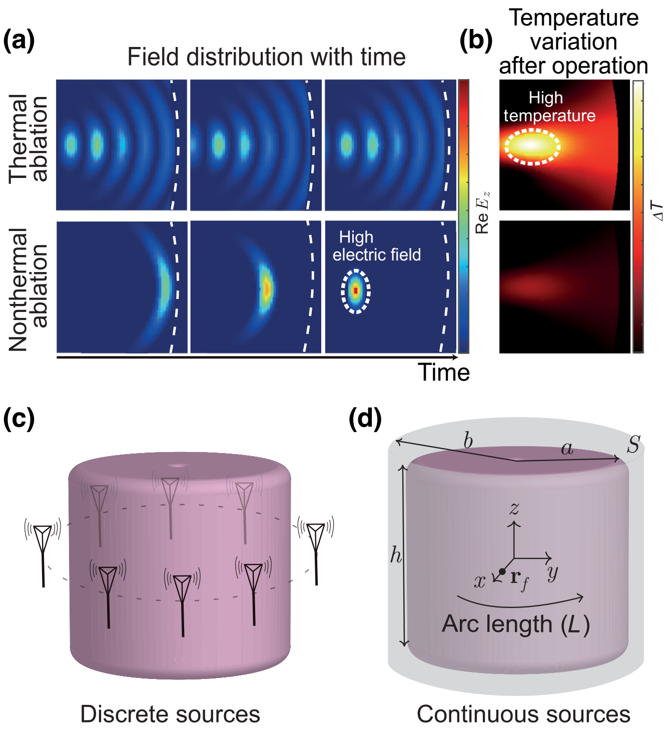

FIG. 1. Conceptual plots of (a) electric field strength according to time and (b) temperature variations of thermal ablation (top) and nonthermal ablation (bottom). (c) Discrete sources and (d) continuously distributed sources on a sheet.

domain cannot be claimed as the global optimum, either [19–21,24]. As a result, various types of source are currently used in practice, with their operating frequency lying in the low-megahertz-to-gigahertz range [16,25] without clear justification for their choices.

In contrast, we find the solution that maximizes the focusing gain from the general source configuration shown in Fig. 1(d). The source is modeled by the continuous electric current density on the surface S surrounding the cylindrical tissue, without any other constraint. By the field-equivalence principle, such a surface current source can represent an arbitrary external source in the aspect of field distribution inside the tissue. Therefore, the resultant focusing gain from the optimization in this work can indeed be the upper bound of the gain.

For the ultimate *thermal* ablation, we show the optimal source should be a monochromatic source with its frequency in the low-gigahertz range. The global bound of the focusing gain reveals significant room for improvement over the existing solutions by 9.1 dB. The physical implementation is realized by a dipole array that mimics the optimal current distribution. We demonstrate that the focusing gain of the dipole array approaches very closely its upper limit.

For the ultimate *nonthermal* ablation, we find a transient current source to induce spatiotemporal focusing of the electric field at a target. The electric field can be focused on scales of a few millimeters and subnanoseconds, surpassing the performance of a primitive dipole-array source by 13.3 dB in its focusing gain.

II. PROBLEM FORMULATION

In this work we model the human body as a cylindrical trunk. The geometric configuration is illustrated in Fig. 1(d), where the radius and the height of the trunk are a and h, respectively. To simplify the analysis, the height h is assumed to be infinite in the field computation. The trunk is considered to be a multilayered medium, where the ith layer has radius ρ_i, complex permittivity ϵ_i, and permeability μ (Fig. 8). The total number of layers, including the external region, is denoted by N. The values of the complex permittivity for each layer of tissue can be obtained from the Cole-Cole tissue model [26].

We aim to find a source outside the body to focus the electric field at a focal point $\mathbf{r}_f$. By the equivalence principle, one can always find a tangential electric current density on a coaxial cylindrical surface S surrounding the body trunk, which creates identical fields with such an optimal one. Therefore, without loss of generality, we may assume the surface-current source $\mathbf{j}(\phi, z, t)$ is confined to the cylindrical surface S with the radius b: $\mathbf{j}(\phi, z, t) = j_\phi(\phi, z, t)\hat{\boldsymbol{\phi}} + j_z(\phi, z, t)\hat{\mathbf{z}}$. The current source creates the electric field $\mathbf{e}(\mathbf{r}, t)$, magnetic field $\mathbf{h}(\mathbf{r}, t)$, and displacement current $\mathbf{j}_D(\mathbf{r}, t)$ within the tissue.

A. Field expression

Within the trunk, the fields can be decomposed into elementary wave functions $\psi_{n,k_z,\omega}(\phi, z, t) = e^{-jn\phi - jk_z z + j\omega t}$ [27,28]:

$$\begin{bmatrix}\mathbf{e}(\mathbf{r}, t)\\ \mathbf{h}(\mathbf{r}, t)\end{bmatrix} = \frac{1}{2\pi}\sum_n \iint dk_z d\omega \begin{bmatrix}\boldsymbol{\mathcal{E}}(\rho, n, k_z, \omega)\psi_{n,k_z,\omega}\\ \boldsymbol{\mathcal{H}}(\rho, n, k_z, \omega)\psi_{n,k_z,\omega}\end{bmatrix}, \tag{1}$$

where $\rho = \sqrt{x^2 + y^2}$, ω is the radial frequency, n is the order of the Bessel equation, and k_z is the wave number in the $\hat{z}$ direction; $k_{i\rho}^2 + k_z^2 = \omega^2\mu\epsilon_i$ in the ith layer. The set $\{\psi_{n,k_z,\omega}\}$ is the orthogonal basis for the Hilbert space Ψ forming the entire Helmholtz-equation solutions for the cylindrical surface with radius ρ.

$\boldsymbol{\mathcal{E}}$ and $\boldsymbol{\mathcal{H}}$ are the spectral representations of the fields that can be computed through the Green's operators $\bar{\boldsymbol{\mathcal{G}}}_E$ and $\bar{\boldsymbol{\mathcal{G}}}_H$ in the spectral domain [27] that map the space of source $\Omega = \{\boldsymbol{\mathcal{J}} | \boldsymbol{\mathcal{J}} = [\mathcal{J}_\phi, \mathcal{J}_z]^T\}$ into Ψ; for example,

$$\boldsymbol{\mathcal{E}} = \bar{\boldsymbol{\mathcal{G}}}_E \boldsymbol{\mathcal{J}} = -\frac{\pi b}{2\omega\epsilon_N}\bar{\mathbf{K}}_i\left(\bar{\mathbf{F}}_{i,n}\overleftarrow{\mathbf{D}}'_s\right)\boldsymbol{\mathcal{J}}. \tag{2}$$

In Eq. (2), the linear operator $\bar{\mathbf{K}}_i$ associates the $\hat{z}$ component of the fields $[\mathcal{E}_z, \mathcal{H}_z]$ with $\boldsymbol{\mathcal{E}}$ in the ith layer, $\bar{\mathbf{F}}_{i,n}$

accounts for the transmission and reflection coefficients of the nth mode in the ith layer, and $\overleftarrow{\mathbf{D}}'_s$ is a differential operator acting on functions to its left to express the emanation of the fields by the currents. $\boldsymbol{\bar{\mathcal{G}}}_E$ is a diagonal operator, which implies the (n, k_z, ω) mode of the current $\boldsymbol{\mathcal{J}}$ emanates only the corresponding (n, k_z, ω) mode of the fields. The expressions for the operators are given in Appendix B.

B. Figures of merit

Two figures of merit are defined to describe the performance of the ablation. One is the spatial (focusing) gain F_s, indicating the performance of thermal ablation, which is the ratio of the time-averaged thermal loss at the target $\mathbf{r}_f$ to the average thermal loss in the body of the volume V:

$$F_s = \frac{\int dt\, \mathbf{e}(\mathbf{r}_f, t) \cdot \mathbf{j}_D(\mathbf{r}_f, t)}{\iint d\mathbf{r}dt\, \mathbf{e}(\mathbf{r}, t) \cdot \mathbf{j}_D(\mathbf{r}, t)/V} = \frac{\int d\omega\, \sigma(\omega)|\mathbf{E}(\mathbf{r}_f, \omega)|^2}{\iint d\mathbf{r}d\omega\, \sigma(\omega)|\mathbf{E}(\mathbf{r}, \omega)|^2/V}, \tag{3}$$

where σ is the conductivity of the tissue and $\mathbf{E}(\mathbf{r}, \omega)$ is the Fourier transform of the electric field $\mathbf{e}(\mathbf{r}, t)$. As we will see, one can deduce the frequency ω_{opt} that maximizes the focusing gain: $\omega_{\text{opt}} = arg\, max_\omega V|\mathbf{E}(\mathbf{r}_f, \omega)|^2/\int_V d\mathbf{r}\, |\mathbf{E}(\mathbf{r}, \omega)|^2$. This makes the spatial gain be bounded by the gain of the monochromatic field at ω_{opt}. Moreover, the characteristics of the cylindrical structure make the electric field strongest along the $\hat{\mathbf{z}}$ direction (see Appendix C), leading to the spatial gain being bounded by

$$F_s \le \frac{V|E_z(\mathbf{r}_f, \omega_{\text{opt}})|^2}{\int_V d\mathbf{r}\, |\mathbf{E}(\mathbf{r}, \omega_{\text{opt}})|^2}. \tag{4}$$

The second figure of merit is the spatiotemporal (focusing) gain F_{ST}, representing the performance of nonthermal ablation. It is the ratio of the instantaneous electric field strength to the overall electric field strength across the body and time:

$$F_{\text{ST}} = \frac{V|e_z(\mathbf{r}_f, t_f = 0)|^2}{\iint d\mathbf{r}dt\, |\mathbf{e}(\mathbf{r}, t)|^2} = \frac{V}{2\pi} \frac{|\int d\omega\, E_z(\mathbf{r}_f, \omega)|^2}{\iint d\mathbf{r}d\omega\, |\mathbf{E}(\mathbf{r}, \omega)|^2}, \tag{5}$$

where we assume the electric field at the target has a peak at time $t_f = 0$ without loss of generality. Likewise, our coordinate system is aligned to make $\phi_f = z_f = 0$ of $\mathbf{r}_f$ to simplify the expression.

C. Source optimization

By applying Parseval's theorem, we can express both Eq. (4) and Eq. (5) as the ratio of inner products in the spectral domain:

$$F = \frac{V}{4\pi^2} \frac{\left|\langle 1, \bar{\mathcal{G}}_{E_z} \boldsymbol{\mathcal{J}} \rangle\right|^2}{\langle \boldsymbol{\mathcal{J}}, \boldsymbol{\bar{\mathcal{L}}} \boldsymbol{\bar{\mathcal{G}}}_E^\dagger \boldsymbol{\bar{\mathcal{G}}}_E \boldsymbol{\mathcal{J}} \rangle}, \tag{6}$$

where $\boldsymbol{\bar{\mathcal{L}}} = \int_0^a \rho d\rho$ is the integral operator along the radial direction. Although the appearances are identical, the difference between the two gains lies in the definition of the inner products.

For the spatial gain F_s, according to Parseval's theorem and Eq. (4), the spatial gain F_s of a monochromatic field with frequency ω_0 is given by

$$\begin{aligned} F_s(\omega_0) &= \frac{V}{4\pi^2} \frac{\left|\sum_n \int_{-\infty}^{\infty} dk_z \mathcal{E}_z(\rho_f, n, k_z, \omega_0)\right|^2}{\int_0^a \rho d\rho\ \sum_n \int dk_z\ |\boldsymbol{\mathcal{E}}(\rho, n, k_z, \omega_0)|^2} \\ &= \frac{V}{4\pi^2} \frac{\left|\langle 1, \bar{\mathcal{G}}_{E_z} \boldsymbol{\mathcal{J}} \rangle_{\Omega_0}\right|^2}{\int_0^a \rho d\rho\ \langle \boldsymbol{\bar{\mathcal{G}}}_E \boldsymbol{\mathcal{J}}, \boldsymbol{\bar{\mathcal{G}}}_E \boldsymbol{\mathcal{J}} \rangle_{\Omega_0}} \\ &= \frac{V}{4\pi^2} \frac{\left|\langle 1, \bar{\mathcal{G}}_{E_z} \boldsymbol{\mathcal{J}} \rangle_{\Omega_0}\right|^2}{\langle \boldsymbol{\mathcal{J}}, \boldsymbol{\bar{\mathcal{L}}} \boldsymbol{\bar{\mathcal{G}}}_E^\dagger \boldsymbol{\bar{\mathcal{G}}}_E \boldsymbol{\mathcal{J}} \rangle_{\Omega_0}}, \end{aligned}$$

where the dependency of $\boldsymbol{\mathcal{J}}$ on the parameters n and k_z is omitted for brevity. The inner product between two tangential fields is defined over the subspace $\Omega_0 \subseteq \Omega$, in which the angular frequency of the source is fixed as ω_0: $\langle \boldsymbol{\mathcal{J}}_1, \boldsymbol{\mathcal{J}}_2 \rangle_{\Omega_0} := \sum_n \int dk_z \left[\mathcal{J}_{1,\phi}^* \mathcal{J}_{2,\phi} + \mathcal{J}_{1,z}^* \mathcal{J}_{2,z}\right]$. By the Cauchy-Schwartz inequality, the above form is maximized when

$$\boldsymbol{\mathcal{J}}_{s,\text{opt}}(n, k_z, \omega_0) = (\boldsymbol{\bar{\mathcal{L}}} \boldsymbol{\bar{\mathcal{G}}}_E^\dagger \boldsymbol{\bar{\mathcal{G}}}_E)^{-1} \bar{\mathcal{G}}_{E_z}^\dagger \Big|_{\omega=\omega_0}, \tag{7}$$

yielding the bound of spatial gain F_s for angular frequency ω_0 as

$$F_{s,\text{opt}}(\omega_0) = \frac{V}{4\pi^2} \langle \bar{\mathcal{G}}_{E_z}^\dagger, \boldsymbol{\mathcal{J}}_{s,\text{opt}} \rangle_{\Omega_0}. \tag{8}$$

For maximization of the spatiotemporal gain, the current source should be chromatic, composed of diverse frequency components: $\boldsymbol{\mathcal{J}} = \boldsymbol{\mathcal{J}}(n, k_z, \omega)$. Similarly as the spatial gain F_s was formulated, the spatiotemporal gain F_{ST} of the (5) can be reformulated as

$$F_{\text{ST}} = \frac{V}{4\pi^2} \frac{\left|\langle 1, \bar{\mathcal{G}}_{E_z} \boldsymbol{\mathcal{J}} \rangle_{\Omega}\right|^2}{\langle \boldsymbol{\mathcal{J}}, \boldsymbol{\bar{\mathcal{L}}} \boldsymbol{\bar{\mathcal{G}}}_E^\dagger \boldsymbol{\bar{\mathcal{G}}}_E \boldsymbol{\mathcal{J}} \rangle_{\Omega}}, \tag{9}$$

where the domain of the inner product is expanded to the entire space Ω: $\langle \boldsymbol{\mathcal{J}}_1, \boldsymbol{\mathcal{J}}_2 \rangle_{\Omega} := 1/2\pi \sum_n \int dk_z \int d\omega \left[\mathcal{J}_{1,\phi}^* \mathcal{J}_{2,\phi} + \mathcal{J}_{1,z}^* \mathcal{J}_{2,z}\right]$. Except for the domain of the inner

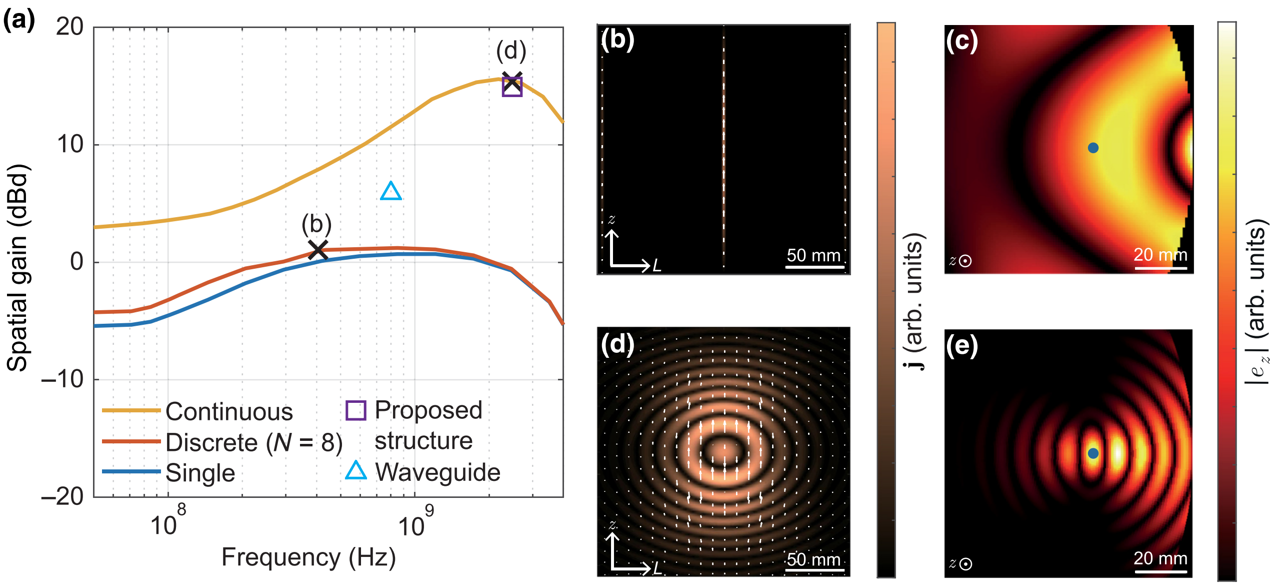

FIG. 2. (a) A spatial gains of various source types according to the operating frequency. The sky-blue triangle and the purple rectangle indicate the gain of the waveguide applicator [29] and the proposed physical structure in this work, respectively. (b) Current distribution on the cylindrical surface S of an array with eight equally spaced dipoles [21] at 400 MHz and (c) its electric field strength in the body. (d) Current distribution of the spatially optimal source on the cylindrical surface S at 2.45 GHz and (e) its electric field strength in the body. The blue dots in (c),(e) indicate the position of the focal point. The fields and currents in (b)–(e) are normalized by their maximum values.

product, the optimization process for F_{ST} is exactly the same as that for F_s, resulting in the optimal source and the bound being

$$\mathcal{J}_{\mathrm{ST,opt}}(n,k_z,\omega) = (\bar{\mathcal{L}}\bar{\mathcal{G}}_E^{\dagger}\bar{\mathcal{G}}_E)^{-1}\bar{\mathcal{G}}_{E_z}^{\dagger}, \tag{10}$$

$$F_{\mathrm{ST,opt}} = \frac{V}{4\pi^2}\langle \bar{\mathcal{G}}_{E_z}^{\dagger}, \mathcal{J}_{\mathrm{ST,opt}}\rangle_{\Omega}. \tag{11}$$

III. NUMERICAL RESULTS

For numerical demonstration, the parameters are set as $\rho_f = 9$ cm, $a = 13$ cm, and $b = 14$ cm and the tissue medium consists of a homogeneous muscle.

A. Thermal ablation

The spatial gain for thermal ablation is normalized by that of a single $\lambda/2$-dipole source at 400 MHz. The gain has the unit of "dBd" to denote that it is a relative gain compared with the dipole source. The spatial gains for various configurations of the source are shown in Fig. 2(a). For a focal depth of 4 ($= a - \rho_f$) cm , the eight-dipole source in Fig. 2(b), of which the excitations are optimized [21], barely increase the spatial gain [the cross on the red curve in Fig. 2(a)]. Figure 2(a) also presents the spatial gain of a highly directive waveguide antenna for hyperthermia at 915 MHz [29]. Compared with them, the optimal continuous source shown in Fig. 2(d) demonstrates room for gain improvement by 14.4 and 9.1 dB, respectively.

The optimal operating frequency ω_{opt} lies in the low-gigahertz range, at which the short wavelength greatly increases the spatial gain. Such a focusing effect obviously appears when one compares the electric field strength for the eight-dipole source at 400 MHz and that for the optimal source shown in Figs. 2(c) and 2(e), respectively. When the above analysis is repeated with various depths from 20 to 120 mm, Fig. 3 shows that the optimal frequency ω_{opt} remains in the low-gigahertz range for all depths. Beyond the low-gigahertz range, the conductivity of tissue abruptly increases and reduces the spatial gain [30].

The maximum depth for hyperthermia can also be investigated by one solving Pennes's bioheat equation [31,32], which governs the temperature T in a living body as

$$\rho_t C_t \frac{dT}{dt} - k\nabla^2 T = h_m + h_b + h_e, \tag{12}$$

where ρ_t, C_t, and k denote the density, specific heat, and thermal conductivity of the tissue, respectively. On the right-hand side, the three nonhomogeneous terms act as either a heat source or a sink. h_m represents heat generated from cell metabolism and is typically regarded as a constant [31]. h_b, which models heat transferred from arterial blood to tissue through a capillary network, depends on the contrast between the tissue temperature and the arterial blood temperature T_a. The thermal effect of the electric field is included in h_e, which models the amount of heat per unit volume during unit time and can be calculated as $h_e(\mathbf{r}) = \sigma(\mathbf{r})|E(\mathbf{r})|^2/2$.

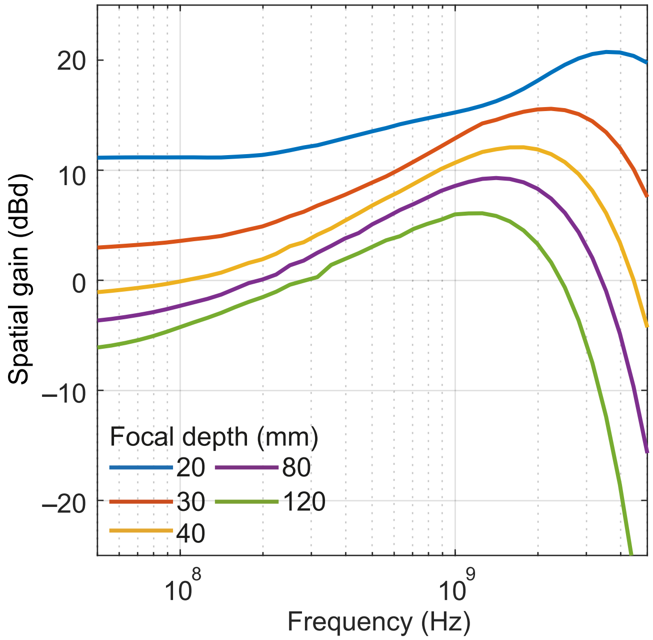

FIG. 3. Spatial gain for various focusing depths.

Pennes's bioheat equation was solved by a custom-developed finite-difference equation solver in a space of $300 \times 300 \times 100\,\mathrm{mm}^3$ with a 2-mm cell size. Table I summarizes the parameter values that we used in the thermal analysis. Surrounding the tissue trunk, we assumed there is a layer of cooling water modeling a bolus at a constant temperature $T_c = 10\,^\circ\mathrm{C}$ that reduces the temperature of the superficial region. Under the assumption that that hyperthermia is to be applied for 1 h [33], Fig. 4 shows the calculated temperature distribution with depth at (a) 30 min and (b) 60 min. The focal depths of hyperthermia range from 20 to 120 mm. The input power, computed as the total loss in the tissue, was adjusted so that the maximum temperature in the tissue was 43 °C at the end of the therapeutic procedure.

We found that the temperature peaks at the desired depth as long as the focal depth is less than 4 cm. For a deeper focal depth, however, the temperature peak arises undesirably at a shallower depth, which implies normal tissues can be impacted before malignant ones by hyperthermia. Therefore, the maximum depth of the target point for hyperthermia is limited to about 4 cm.

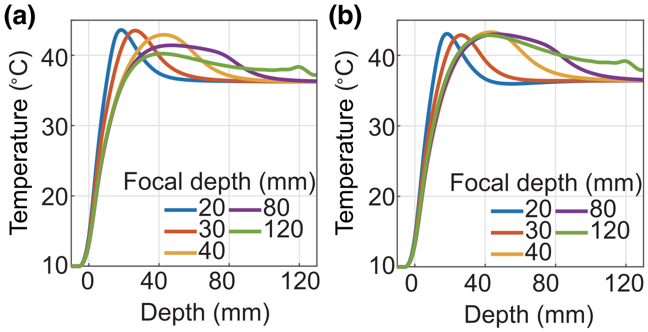

FIG. 4. Temperature distribution with different focal depths after application of hyperthermia for (a) 30 min and (b) 60 min.

TABLE I. Parameters for Pennes's bioheat equation.

Parameter	Notation	Value	Unit abbreviation
Mass density	ρ_t	1.004×10^3	kg m^{-3}
Specific heat (muscle)	C_t	8.2×10^{-1}	kcal $\mathrm{kg}^{-1}\,^\circ\mathrm{C}^{-1}$
Thermal conductivity (muscle)	k	1.5×10^{-4}	kcal $\mathrm{s}^{-1}\,\mathrm{m}^{-1}\,^\circ\mathrm{C}^{-1}$
Rate of metabolic heat production per unit volume	h_m	1×10^{-1}	kcal $\mathrm{s}^{-1}\,\mathrm{m}^{-3}$
Rate of heat transfer per unit volume of tissue	h_b	$0.2162\times (T_a - T)$	kcal $\mathrm{s}^{-1}\,\mathrm{m}^{-3}$
Arterial blood temperature	T_a	36.25	°C

B. Nonthermal ablation

We numerically demonstrate the bound of spatiotemporal gain for nonthermal ablation under the same configuration of (ρ_f, a, b) as the spatial gain. Figure 5(a) shows the optimal source should flow inward radially, which makes the electric field spatially focused in a region with a size of $5 \times 10 \times 10\,\mathrm{mm}^3$ at $t = 0$ ns, visualized in Figs. 5(b) and 5(c). In contrast to the field generated by the spatially optimal source, the field fades out after peaking for a few tenths of a nanosecond [Fig. 5(d)] to minimize the total loss in tissue across time. The subnanosecond duration of the peak indicates that the spatiotemporally optimal field is also dominated by low-gigahertz components like the spatially optimal field. A higher-frequency component then does not help to increase the gain F_{ST} because it severely attenuates before it reaches the target.

The performance of this optimal source can be compared with that of traditional sources. We chose an eight-dipole array [21] around the trunk to compare the performance. The excitations of the eight dipoles were optimized to yield the highest spatiotemporal gain. Figure 6 shows the electric field from the eight-dipole array as time progresses. While the field is temporally focused within a tenth of a nanosecond near $t = 0$ ns, the spatial focusing is very poor with the eight-dipole array. Therefore, the spatiotemporal gain of the optimal source is 13.3 dB higher than that of the eight-dipole array.

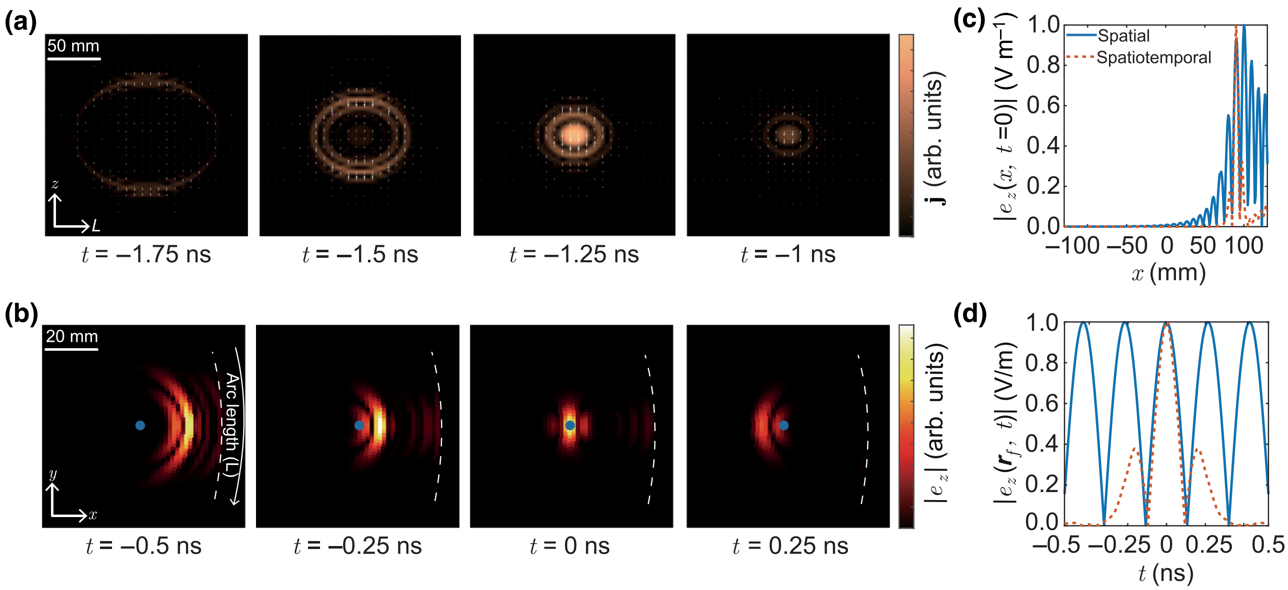

FIG. 5. (a) Current distribution of the spatiotemporally optimal source and (b) its instantaneous electric field in the body over time. The blue dots indicate the focal point $\mathbf{r}_f$. (c) Instantaneous electric field strength along the x axis at time $t = t_f$ (0 ns) and (d) versus time at the focal point $\mathbf{r}_f$ for the spatially and spatiotemporally optimal sources. The fields and currents are normalized by their maximum values.

IV. PHYSICAL IMPLEMENTATION

In this section we investigate the physical implementation of the optimal current distribution for thermal ablation. We demonstrate the developmental procedure for the physical antenna that mimics the optimal distribution targeting a depth of 4 cm. As observed in Fig. 2(d), the $\hat{z}$ component dominates in the optimal current distribution. To synthesize it, we use an 11×11

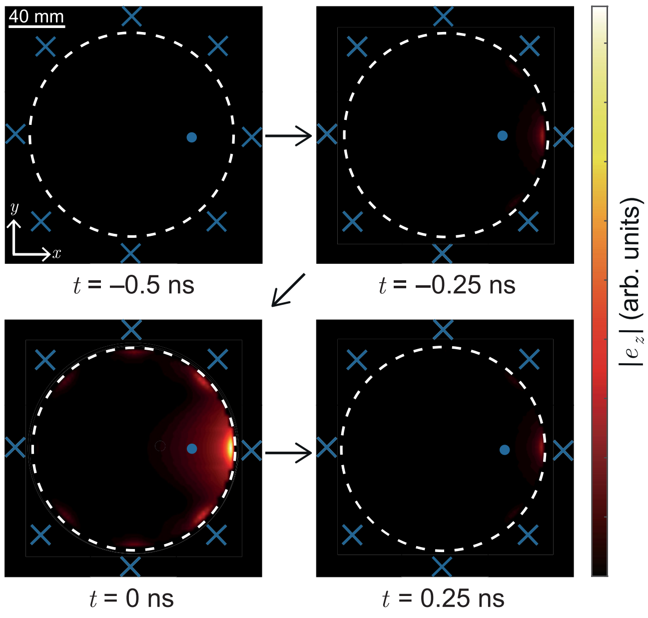

FIG. 6. Electric field strength from the eight-Hertzian-dipole array versus time. The focal point and the positions of dipoles are denoted by the blue dot and the blue crosses, respectively. The field is normalized by its maximum value.

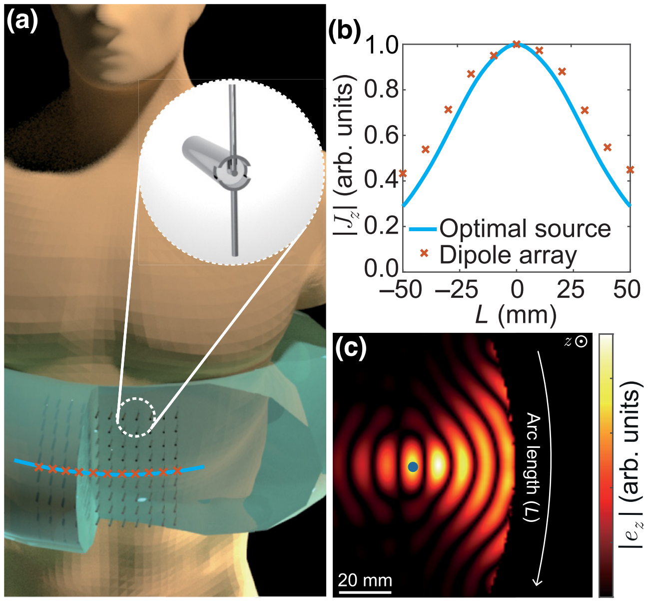

FIG. 7. (a) Physical implementation of the source as an 11×11 balanced, half-wavelength dipole array (inset) immersed in a water bolus. (b) Magnitude of excitation coefficients (red crosses) of the dipole array and the spatially optimal source (blue curve) along an arc of length L at $z = 0$. (c) Electric field strength generated by the proposed 11×11 dipole array. The blue dot indicates the focal point $\mathbf{r}_f$. The fields and currents are normalized by their maximum values.

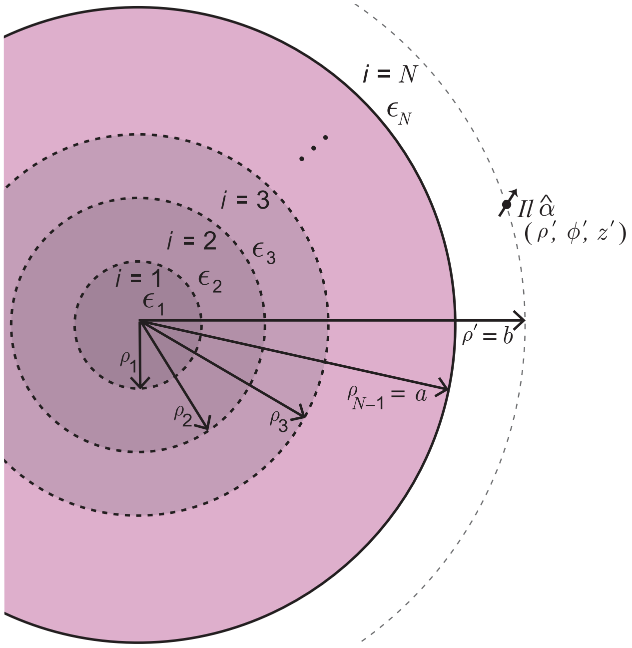

FIG. 8. A point source outside a multilayered medium. Multiple reflections and transmissions at the interfaces must be considered in field computation.

phased-array antenna over an area of 10 × 10 cm^2, depicted in Fig. 7(a), where each element is a balanced, half-wavelength dipole antenna [6 mm long at 2.45 GHz in water; Fig. 7(a), inset] along the $\hat{z}$ direction. The spacing between the elements is set to be 10 mm.

The excitation coefficients of the dipole array are determined as follows. From the principle of superposition, the net electric field can be expressed as the excitation coefficients multiplied by a field matrix. The component of the field matrix describes the electric field distribution of each dipole and can be obtained by a commercial electromagnetic simulator, CST MICROWAVE STUDIO. On the basis of the field matrix, the excitation coefficients of the array can be numerically determined to maximize the field strength at the focal point for a given total loss in the tissue [19,20,34]. Figure 7(b) shows the coefficients obtained as such along $z = 0$ (the red crosses), closely following the optimal solution over the continuous domain (the blue curve). The field distribution [Fig. 7(c)] inside the body caused by the dipole array also reveals the focusing effect approximates the optimal one in Fig. 2(e), achieving a focusing gain [the purple square in Fig. 2(a)] only 0.4 dB below the upper bound. As marked in Fig. 2(a), this is performance far exceeds that in previous work.

V. CONCLUSION

Previously, the domains of the optimization for hyperthermia were inherently restricted, failing to claim the global optimum. In this work we performed optimization over a hypothetical, continuous current density, deducing the globally optimal current distribution and addressing the ultimate performance for both thermal ablation and nonthermal ablation.

As a numerical example, the performance of the ablations was demonstrated when the focal depth is 4 cm. The bound of the spatial gain reveals room for improvement over existing solutions by 9.1 dB. Likewise, the bound of the spatiotemporal gain exceeds the gain of a primitive source, the equally spaced eight-dipole array, by 13.3 dB.

ACKNOWLEDGMENTS

This work was, in part, supported by the Institute of Information & communications Technology Planning & Evaluation (IITP) grant funded by Korea government (MSIT) (Grants No. IITP-2021-0-02046 and No. RS-2024-00393808), in part supported by the National Research Foundation of Korea (Grants No. NRF-2018R1A6A1A03025708 and No. NRF-2023R1A2C2004236).

APPENDIX A: FIELDS GENERATED BY A POINT SOURCE

We wish to express the fields in a trunk generated by a continuous surface current $\mathbf{J}$ on the cylindrical surface S. To do so, it is essential to understand the fields generated by a point source [27]. For completeness of the paper, the expressions for the fields generated by a point source are given in this appendix.

In a homogeneous space with permittivity ϵ, when a dipole point source Il at $\mathbf{r}'$ points in the $\hat{\boldsymbol{\alpha}} = \left[\alpha_\rho, \alpha_\phi, \alpha_z\right]^T$ direction, one can express the z components of the fields as

$$E_z = \frac{-jIl}{\omega\epsilon}\left[\hat{\mathbf{z}}\cdot\hat{\boldsymbol{\alpha}}k^2 + \frac{\partial}{\partial z'}\nabla'\cdot\hat{\boldsymbol{\alpha}}\right]\frac{e^{-jk|\mathbf{r}-\mathbf{r}'|}}{4\pi|\mathbf{r}-\mathbf{r}'|}, \tag{A1}$$

$$H_z = -Il\hat{\boldsymbol{\alpha}}\cdot\hat{\mathbf{z}}\times\nabla'\frac{e^{-jk|\mathbf{r}-\mathbf{r}'|}}{4\pi|\mathbf{r}-\mathbf{r}'|}. \tag{A2}$$

On the other hand, according to the Sommerfeld integral and the addition theorem, the operand $e^{-jk|\mathbf{r}-\mathbf{r}'|}/(4\pi|\mathbf{r}-\mathbf{r}'|)$ can be decomposed into Bessel and Hankel functions:

$$\frac{e^{-jk|\mathbf{r}-\mathbf{r}'|}}{4\pi|\mathbf{r}-\mathbf{r}'|} = \sum_{n=-\infty}^{\infty}\frac{-je^{-jn(\phi-\phi')}}{8\pi}\int_{-\infty}^{\infty}dk_z \times e^{-jk_z(z-z')}J_n(k_\rho\rho_<)H_n^{(2)}(k_\rho\rho_>), \tag{A3}$$

where $\rho_<$ and $\rho_>$ refer to the greater one and the smaller one among ρ and ρ', respectively.

Substituting Eq. (A3) into Eqs. (A1) and (A2), one gets the following field expressions for the z component:

$$\begin{bmatrix} E_z \\ H_z \end{bmatrix} = -\frac{Il}{8\pi\omega\epsilon} \sum_{n=-\infty}^{\infty} e^{-jn(\phi-\phi')} \int_{-\infty}^{\infty} dk_z \\ \times e^{-jk_z(z-z')} J_n(k_\rho \rho_<) H_n^{(2)}(k_\rho \rho_>) \overleftarrow{\mathbf{D}} \hat{\boldsymbol{\alpha}}, \qquad \text{(A4)}$$

where $\overleftarrow{\mathbf{D}}'$ is a differential operator that acts on functions to its left. For the reader's reference, the $e^{jn\phi'+jk_z z'}$ dependency of the fields makes the operator act on the fields as

$$B_n(k_\rho \rho') \overleftarrow{\mathbf{D}}' = \begin{bmatrix} -k_\rho k_z B_n'(k_\rho \rho') & -\frac{n\omega\epsilon}{\rho'} B_n(k_\rho \rho') \\ -n\frac{k_z}{\rho'} B_n(k_\rho \rho') & -j\omega\epsilon k_\rho B_n'(k_\rho \rho') \\ \left(k^2 - k_z^2\right) B_n(k_\rho \rho') & 0 \end{bmatrix}^T,$$

where B_n is either a J_n function or an $H_n^{(2)}$ function.

For our purpose of tissue ablation, there is a trunk-shaped medium with radius a, and the point source Il is located in the outermost (Nth) layer at $\mathbf{r}'$ ($\rho' > a$) in the $\hat{\boldsymbol{\alpha}}$ direction (Fig. 8). We have to account for the transmission and the reflection of the wave at the cylindrical interface. In general, the fields in the ith region are expressed as

$$\begin{bmatrix} E_z \\ H_z \end{bmatrix} = -\frac{Il}{8\pi\omega\epsilon_N} \sum_{n=-\infty}^{\infty} e^{-jn(\phi-\phi')} \int_{-\infty}^{\infty} dk_z \\ \times e^{-jk_z(z-z')} \bar{\mathbf{F}}_{i,n}(\rho, b) \overleftarrow{\mathbf{D}}' \hat{\boldsymbol{\alpha}}. \qquad \text{(A5)}$$

The operator $\bar{\mathbf{F}}_{i,n}(\rho, b)$ accounts for the reflection and transmission of the fields in the ith layer and can be computed as follows.

First, one defines the generalized reflection matrices $\widetilde{\overline{\mathbf{R}}}_{i,i-1}$ and $\widetilde{\overline{\mathbf{R}}}_{i,i+1}$, which include the physics of multiple reflections in the ith layer occurring at the interface with the $(i-1)$th layer and the $(i+1)$th layer, respectively [27]:

$$\widetilde{\overline{\mathbf{R}}}_{i,i-1} = \overline{\mathbf{R}}_{i,i-1} + \overline{\mathbf{T}}_{i-1,i} \cdot \widetilde{\overline{\mathbf{R}}}_{i-1,i-2} \\ \times (\bar{\mathbf{I}} - \overline{\mathbf{R}}_{i-1,i} \cdot \widetilde{\overline{\mathbf{R}}}_{i-1,i-2})^{-1} \cdot \overline{\mathbf{T}}_{i,i-1}, \qquad \text{(A6)}$$

$$\widetilde{\overline{\mathbf{R}}}_{i,i+1} = \overline{\mathbf{R}}_{i,i+1} + \overline{\mathbf{T}}_{i+1,i} \cdot \widetilde{\overline{\mathbf{R}}}_{i+1,i+2} \\ \times (\bar{\mathbf{I}} - \overline{\mathbf{R}}_{i+1,i} \cdot \widetilde{\overline{\mathbf{R}}}_{i+1,i+2})^{-1} \cdot \overline{\mathbf{T}}_{i,i+1}, \qquad \text{(A7)}$$

where $\bar{\mathbf{I}}$ is the identity matrix, and $\overline{\mathbf{T}}_{i,j}$ and $\overline{\mathbf{R}}_{i,j}$ are local transmission and reflection matrices for waves propagating from the ith layer to the jth layer. Starting from the initial condition $\widetilde{\overline{\mathbf{R}}}_{1,0} = 0$ and $\widetilde{\overline{\mathbf{R}}}_{N,N+1} = 0$, the recursive definitions of Eqs. (A6) and (A7) are valid. Additionally, the generalized transmission matrix $\widetilde{\overline{\mathbf{T}}}_{N,i}$ is defined to explain the transmission of a wave from the Nth layer to the ith layer involving multiple reflections:

$$\widetilde{\overline{\mathbf{T}}}_{N,i} = \overline{\mathbf{S}}_{i+1,i} \cdot \overline{\mathbf{S}}_{i+2,i+1} \cdot \cdots \cdot \overline{\mathbf{S}}_{N,N-1},$$

where $\overline{\mathbf{S}}_{i,i-1} = (\bar{\mathbf{I}} - \overline{\mathbf{R}}_{i-1,i} \cdot \widetilde{\overline{\mathbf{R}}}_{i-1,i-2})^{-1} \cdot \overline{\mathbf{T}}_{i,i-1}$. Matching boundary condition of each layer yields $\bar{\mathbf{F}}_{i,n}(\rho, b)$ of the ith layer ($\rho_{i-1} < \rho < \rho_i$) as

$$\bar{\mathbf{F}}_{i,n}(\rho, b) = H_n^{(2)}(k_{N\rho} b) \cdot \left[J_n(k_{i\rho}\rho)\bar{\mathbf{I}} + H_n^{(2)}(k_{i\rho}\rho)\widetilde{\overline{\mathbf{R}}}_{i,i-1}\right] \\ \times \widetilde{\overline{\mathbf{M}}}_i \cdot \widetilde{\overline{\mathbf{T}}}_{N,i}, \qquad \text{(A8)}$$

where $\widetilde{\overline{\mathbf{M}}}_i = (\bar{\mathbf{I}} - \widetilde{\overline{\mathbf{R}}}_{i,i+1} \cdot \widetilde{\overline{\mathbf{R}}}_{i,i-1})^{-1}$.

In the case of a single layer ($N = 2$), which we used as a numerical example, it is sufficient to consider the field expression in region 1. With $\widetilde{\overline{\mathbf{R}}}_{1,0} = 0$, the expression for the operator $\bar{\mathbf{F}}_{i,n}$ in Eq. (A8) reduces to

$$\bar{\mathbf{F}}_{1,n}(\rho, b) = J_n(k_{1\rho}\rho)\widetilde{\overline{\mathbf{T}}}_{21} H_n^{(2)}(k_{2\rho} b).$$

Within the trunk of a single layer, there is only a standing wave $J_n(k_{1\rho}\rho)$ as expected. For the reader's reference, in this single-layer configuration, the generalized transmission matrix is

$$\widetilde{\overline{\mathbf{T}}}_{21} = \frac{2\omega}{\pi k_{2\rho}^2 a} \overline{\mathbf{D}}^{-1} \begin{bmatrix} \epsilon_2 & 0 \\ 0 & -\mu \end{bmatrix},$$

where

$$\overline{\mathbf{D}} = \overline{\mathbf{J}}_n(k_{1\rho} a) H_n^{(2)}(k_{2\rho} a) - \overline{\mathbf{H}}_n^{(2)}(k_{2\rho} a) J_n(k_{1\rho} a)$$

and

$$\overline{\mathbf{J}}_n(k_{i\rho} a) = \frac{1}{k_{i\rho}^2 a} \begin{bmatrix} -j\omega\epsilon_i k_{i\rho} a J_n'(k_{i\rho} a) & -nk_z J_n(k_{i\rho} a) \\ -nk_z J_n(k_{i\rho} a) & j\omega\mu k_{i\rho} a J_n'(k_{i\rho} a) \end{bmatrix},$$

$$\overline{\mathbf{H}}_n^{(2)}(k_{i\rho} a) = \frac{1}{k_{i\rho}^2 a} \begin{bmatrix} -j\omega\epsilon_i k_{i\rho} a H_n^{(2)\prime}(k_{i\rho} a) & -nk_z H_n^{(2)}(k_{i\rho} a) \\ -nk_z H_n^{(2)}(k_{i\rho} a) & j\omega\mu k_{i\rho} a H_n^{(2)\prime}(k_{i\rho} a) \end{bmatrix}.$$

APPENDIX B: FIELDS GENERATED BY A CONTINUOUS SOURCE

From the principle of superposition, the fields inside the body generated by a continuous source $\mathbf{J}(\phi', z')$ are expressed as

$$\begin{bmatrix} E_z \\ H_z \end{bmatrix} = -\frac{1}{8\pi\omega\epsilon_N}\int_{-\pi}^{\pi} b\,d\phi' \int_{-\infty}^{\infty} dz' \sum_{n=-\infty}^{\infty} e^{-jn(\phi-\phi')} \times \int_{-\infty}^{\infty} dk_z\, e^{-jk_z(z-z')}\bar{\mathbf{F}}_{i,n}(\rho, b)\,\overleftarrow{\mathbf{D}}'_s \begin{bmatrix} J_\phi \\ J_z \end{bmatrix}, \tag{B1}$$

where $\overleftarrow{\mathbf{D}}'_s$ is the transverse components of the operator $\overleftarrow{\mathbf{D}}'$, which excludes the ρ component. On the other hand, by the Fourier transform and the Fourier series, the current source can be expressed as

$$\begin{bmatrix} J_\phi(\phi', z') \\ J_z(\phi', z') \end{bmatrix} = \frac{1}{2\pi}\sum_n \int_{-\infty}^{\infty} dk_z e^{-jn\phi' - jk_z z'} \begin{bmatrix} \mathcal{J}_\phi(n, k_z) \\ \mathcal{J}_z(n, k_z) \end{bmatrix},$$

and inversely,

$$\begin{bmatrix} \mathcal{J}_\phi \\ \mathcal{J}_z \end{bmatrix} = \frac{1}{2\pi}\int_{-\pi}^{\pi} d\phi' \int_{-\infty}^{\infty} dz' e^{+jn\phi' + jk_z z'} \begin{bmatrix} J_\phi \\ J_z \end{bmatrix}. \tag{B2}$$

Likewise, the fields can be decomposed in the spectral domain as

$$\begin{bmatrix} E_z \\ H_z \end{bmatrix} = \frac{1}{2\pi}\sum_{n=-\infty}^{\infty}\int_{-\infty}^{\infty} dk_z e^{-jn\phi - jk_z z} \begin{bmatrix} \mathcal{E}_z \\ \mathcal{H}_z \end{bmatrix}, \tag{B3}$$

where $\mathcal{E}_z$ and $\mathcal{H}_z$ are the spectral components of the electric and magnetic fields, respectively. The dependency of E_z and H_z on (ρ, ϕ, z) and that of $\mathcal{E}$ and $\mathcal{H}$ on (ρ, n, k_z) are omitted for brevity.

Switching the order of integrals and rearranging the terms in Eq. (B1) yields

$$\begin{bmatrix} E_z \\ H_z \end{bmatrix} = -\frac{b}{4\omega\epsilon_N}\sum_{n=-\infty}^{\infty}\int_{-\infty}^{\infty} dk_z e^{-jn\phi} e^{-jk_z z} \times \frac{1}{2\pi}\int_{-\pi}^{\pi} d\phi' \int_{-\infty}^{\infty} dz'\; e^{+jn\phi'} e^{+jk_z z'} \times \bar{\mathbf{F}}_{i,n}(\rho, b)\,\overleftarrow{\mathbf{D}}'_s \begin{bmatrix} J_\phi(\phi', z') \\ J_z(\phi', z') \end{bmatrix}. \tag{B4}$$

Since the term $\bar{\mathbf{F}}_{i,n}\overleftarrow{\mathbf{D}}'$ is independent of ϕ' and z', by Eq. (B2), the fields can be represented in terms of the spectral current densities $\mathcal{J}_\phi$ and $\mathcal{J}_z$ as

$$\begin{bmatrix} E_z \\ H_z \end{bmatrix} = -\frac{b}{4\omega\epsilon_N}\sum_n \int_{-\infty}^{\infty} dk_z e^{-jn\phi - jk_z z} \times \bar{\mathbf{F}}_{i,n}(\rho, b)\,\overleftarrow{\mathbf{D}}'_s \begin{bmatrix} \mathcal{J}_\phi(n, k_z) \\ \mathcal{J}_z(n, k_z) \end{bmatrix}. \tag{B5}$$

Comparing the above equation with Eq. (B3), we find a multiplicative relation between the fields and the current source in the spectral domain as

$$\begin{bmatrix} \mathcal{E}_z(\rho, n, k_z) \\ \mathcal{H}_z(\rho, n, k_z) \end{bmatrix} = -\frac{\pi b}{2\omega\epsilon_N}\bar{\mathbf{F}}_{i,n}(\rho, b)\,\overleftarrow{\mathbf{D}}'_s \begin{bmatrix} \mathcal{J}_\phi(n, k_z) \\ \mathcal{J}_z(n, k_z) \end{bmatrix}. \tag{B6}$$

This yields the Green's function operator $\bar{\mathcal{G}}_{E_z}$ for the z component of electric field as

$$\bar{\mathcal{G}}_{E_z} = -\frac{\pi b}{2\omega\epsilon_N}[1, 0]\left(\bar{\mathbf{F}}_{i,n}\overleftarrow{\mathbf{D}}'_s\right). \tag{B7}$$

Lastly, the transverse components of the electric fields in cylindrical coordinates can be determined from the following equations:

$$\begin{bmatrix} \mathcal{E}_\rho \\ \mathcal{E}_\phi \end{bmatrix} = \frac{1}{k_{i\rho}^2}\left[-jk_z\nabla_s\mathcal{E}_z + j\omega\mu\hat{\mathbf{z}}\times\nabla_s\mathcal{H}_z\right], \tag{B8}$$

where ∇_s is the transverse components of the operator ∇, which excludes the ρ component. In the operator formulation, this is equivalent to

$$\boldsymbol{\mathcal{E}} = \begin{bmatrix} \mathcal{E}_\rho \\ \mathcal{E}_\phi \\ \mathcal{E}_z \end{bmatrix} = \bar{\mathbf{K}}_i \begin{bmatrix} \mathcal{E}_z \\ \mathcal{H}_z \end{bmatrix} = -\frac{\pi b}{2\omega\epsilon_N}\bar{\mathbf{K}}_i\left(\bar{\mathbf{F}}_{i,n}\overleftarrow{\mathbf{D}}'_s\right)\begin{bmatrix} \mathcal{J}_\phi(n, k_z) \\ \mathcal{J}_z(n, k_z) \end{bmatrix}, \tag{B9}$$

where $\bar{\mathbf{K}}_i$ is the differential operator associated with Eq. (B8):

$$\bar{\mathbf{K}}_i = \frac{1}{k_{i\rho}^2}\begin{bmatrix} -jk_z\frac{\partial}{\partial\rho} & -\frac{n\omega\mu}{\rho} \\ -\frac{nk_z}{\rho} & j\omega\mu\frac{\partial}{\partial\rho} \\ k_{i\rho}^2 & 0 \end{bmatrix}. \tag{B10}$$

Finally, we have the Green's function operator $\bar{\boldsymbol{\mathcal{G}}}_E$ that relates the electric fields $\boldsymbol{\mathcal{E}}$ to the current source $\boldsymbol{\mathcal{J}} = [\mathcal{J}_\phi, \mathcal{J}_z]^T$ in Eq. (2):

$$\bar{\boldsymbol{\mathcal{G}}}_E = -\frac{\pi b}{2\omega\epsilon_N}\bar{\mathbf{K}}_i\left(\bar{\mathbf{F}}_{i,n}\overleftarrow{\mathbf{D}}'_s\right). \tag{B11}$$

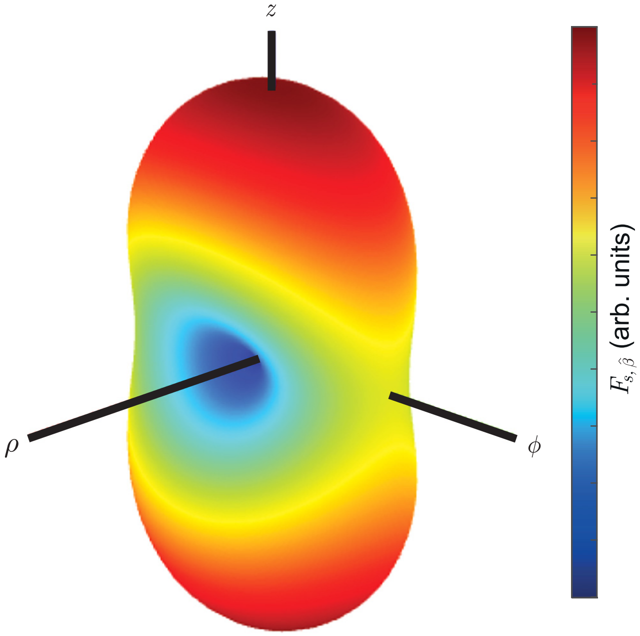

FIG. 9. Upper bound of spatial gain $F_{s,\hat{\boldsymbol{\beta}}}$ depending on the direction of $\hat{\boldsymbol{\beta}}$ for $\rho_f = 9$ cm, $a = 13$ cm, and $b = 14$ cm. The spatial gain is normalized by its maximum value.

APPENDIX C: SOURCE OPTIMIZATION TO MAXIMIZE $|\mathbf{E}(\mathbf{r}_f)|$ IN OTHER DIRECTIONS

To yield the best focusing performance, one should exploit the vector nature of the electric field [35]. In general, the spatial gain of the electric field in an arbitrary direction $\hat{\boldsymbol{\beta}}$, where $\hat{\boldsymbol{\beta}}$ is a unit vector, can be defined as

$$F_{s,\hat{\boldsymbol{\beta}}} = \frac{V|\hat{\boldsymbol{\beta}} \cdot \mathbf{E}(\mathbf{r}_f)|^2}{\int_V d\mathbf{r}\ |\mathbf{E}(\mathbf{r})|^2}.$$

As a numerical example, the upper bound of $F_{s,\hat{\boldsymbol{\beta}}}$ is computed for each direction of $\hat{\boldsymbol{\beta}}$ when $\rho_f = 9$ cm, $a = 13$ cm, and $b = 14$ cm (Fig. 9). Figure 9 shows that $F_{s,\hat{\boldsymbol{\beta}}}$ is maximized when $\hat{\boldsymbol{\beta}}$ is in the $\hat{\mathbf{z}}$ direction. The deep position of the focal point makes the transverse ($\hat{\mathbf{z}}$) component much greater than the longitudinal ($\hat{\boldsymbol{\rho}}$) component. Therefore, the spatial gain is maximized along the $\hat{\mathbf{z}}$ direction in our work.

[1] C. Pfeiffer and A. Grbic, Metamaterial huygens' surfaces: Tailoring wave fronts with reflectionless sheets, Phys. Rev. Lett. **110**, 197401 (2013).

[2] A. Grbic and G. V. Eleftheriades, Overcoming the diffraction limit with a planar left-handed transmission-line lens, Phys. Rev. Lett. **92**, 117403 (2004).

[3] J. B. Pendry, Negative refraction makes a perfect lens, Phys. Rev. Lett. **85**, 3966 (2000).

[4] N. Fang, H. Lee, C. Sun, and X. Zhang, Sub-diffraction-limited optical imaging with a silver superlens, Science **308**, 534 (2005).

[5] G. Timp, R. Behringer, D. Tennant, J. Cunningham, M. Prentiss, and K. Berggren, Using light as a lens for submicron, neutral-atom lithography, Phys. Rev. Lett. **69**, 1636 (1992).

[6] J. Stang, M. Haynes, P. Carson, and M. Moghaddam, A preclinical system prototype for focused microwave thermal therapy of the breast, IEEE Trans. Biomed. Eng. **59**, 2431 (2012).

[7] F. Yang, B. O. Raeker, D. T. Nguyen, J. D. Miller, Z. Xiong, A. Grbic, and J. S. Ho, Antireflection and wavefront manipulation with cascaded metasurfaces, Phys. Rev. Appl. **14**, 064044 (2020).

[8] J. S. Ho, B. Qiu, Y. Tanabe, A. J. Yeh, S. Fan, and A. S. Poon, Planar immersion lens with metasurfaces, Phys. Rev. B **91**, 125145 (2015).

[9] S. Kim, J. S. Ho, and A. S. Poon, Wireless power transfer to miniature implants: Transmitter optimization, IEEE Trans. Antennas Propag. **60**, 4838 (2012).

[10] S. Kim, J. S. Ho, and A. S. Poon, Midfield wireless powering of subwavelength autonomous devices, Phys. Rev. Lett. **110**, 203905 (2013).

[11] B. Hildebrandt, P. Wust, O. Ahlers, A. Dieing, G. Sreenivasa, T. Kerner, R. Felix, and H. Riess, The cellular and molecular basis of hyperthermia, Crit. Rev. Oncol. Hematol. **43**, 33 (2002).

[12] I. C. H. Group, C. C. Vernon, J. W. Hand, S. B. Field, D. Machin, J. B. Whaley, J. van der Zee, W. L. van Putten, G. C. van Rhoon, J. D. van Dijk, *et al.*, Radiotherapy with or without hyperthermia in the treatment of superficial localized breast cancer: Results from five randomized controlled trials, Int. J. Radiat. Oncol. Biol. Phys. **35**, 731 (1996).

[13] Z. Vujaskovic, D. W. Kim, E. Jones, L. Lan, L. McCall, M. W. Dewhirst, O. Craciunescu, P. Stauffer, V. Liotcheva, A. Betof, *et al.*, A phase i/ii study of neoadjuvant liposomal doxorubicin, paclitaxel, and hyperthermia in locally advanced breast cancer, Int. J. Hyperthermia **26**, 514 (2010).

[14] A. Verma, S. J. Asivatham, T. Deneke, Q. Castellvi, and R. E. Neal, Primer on pulsed electrical field ablation: Understanding the benefits and limitations, Circ.: Arrhythmia Electrophysiol. **14**, e010086 (2021).

[15] P. R. Stauffer, in *Matching the Energy Source to the Clinical Need: A Critical Review* (SPIE, Bellingham, Washington, 2000), Vol. 10297, p. 321.

[16] P. Wust, B. Hildebrandt, G. Sreenivasa, B. Rau, J. Gellermann, H. Riess, R. Felix, and P. Schlag, Hyperthermia in combined treatment of cancer, Lancet Oncol. **3**, 487 (2002).

[17] W. Gee, S.-W. Lee, N. K. Bong, C. A. Cain, R. Mittra, and R. L. Magin, Focused array hyperthermia applicator: Theory and experiment, IEEE Trans. Biomed. Eng. **BME-31**, 38 (1984).

[18] H. Ling and S.-W. Lee, Focusing of electromagnetic waves through a dielectric interface, JOSA A **1**, 965 (1984).

[19] M. Seebass, R. Beck, J. Gellermann, J. Nadobny, and P. Wust, Electromagnetic phased arrays for regional hyperthermia: Optimal frequency and antenna arrangement, Int. J. Hyperthermia **17**, 321 (2001).

[20] D. P. Keith, S. Geimer, T. Jingwu, and E. B. William, Optimization of pelvic heating rate distributions with electromagnetic phased arrays, Int. J. Hyperthermia **15**, 157 (1999).

[21] S. Lee, S. Han, W. Song, K.-J. Lee, and S. Kim, Discrete source optimization for microwave hyperthermia using quantum annealing, IEEE Antennas Wirel. Propag. Lett. **23** (3), 1095 (2023).

[22] A. Boag and Y. Leviatan, Optimal excitation of multiapplicator systems for deep regional hyperthermia, IEEE Trans. Biomed. Eng. **37**, 987 (1990).

[23] A. Boag, Y. Leviatan, and A. Boag, Analysis and optimization of waveguide multiapplicator hyperthermia systems, IEEE Trans. Biomed. Eng. **40**, 946 (1993).

[24] H. Ling, S.-W. Lee, and W. Gee, Frequency optimization of focused microwave hyperthermia applicators, Proc. IEEE **72**, 224 (1984).

[25] A. Vander Vorst, A. Rosen, and Y. Kotsuka, *RF/Microwave Interaction with Biological Tissues* (John Wiley & Sons, Hoboken, New Jersey, 2006).

[26] S. Gabriel, R. Lau, and C. Gabriel, The dielectric properties of biological tissues: III. Parametric models for the dielectric spectrum of tissues, Phys. Med. Biol. **41**, 2271 (1996).

[27] W. C. Chew, *Waves and Fields in Inhomogeneous Media* (IEEE Press, New York, 1995), Vol. 16.

[28] R. F. Harrington, *Time-Harmonic Electromagnetic Fields* (IEEE Press, New York, 2001).

[29] J. Song, X. Sun, Y. Du, Q. Wu, M. Niu, C. Fu, L. Tan, X. Ren, L. Chen, and X. Meng, Micro-opening ridged waveguide tumor hyperthermia antenna combined with microwave-sensitive MOF material for tumor microwave hyperthermia therapy, ACS Appl. Bio Mater. **5**, 4154 (2022).

[30] A. S. Y. Poon, S. O'Driscoll, and T. H. Meng, Optimal frequency for wireless power transmission into dispersive tissue, IEEE Trans. Antennas Propag. **58**, 1739 (2010).

[31] H. H. Pennes, Analysis of tissue and arterial blood temperatures in the resting human forearm, J. Appl. Physiol. **1**, 93 (1948).

[32] E. H. Wissler, Pennes' 1948 paper revisited, J. Appl. Physiol. **85**, 35 (1998).

[33] P. J. Rietveld, W. L. van Putten, J. van der Zee, and G. C. van Rhoon, Comparison of the clinical effectiveness of the 433 MHz lucite cone applicator with that of a conventional waveguide applicator in applications of superficial hyperthermia, Int. J. Radiat. Oncol. Biol. Phys. **43**, 681 (1999).

[34] S. Kim, J. S. Ho, L. Y. Chen, and A. S. Poon, Wireless power transfer to a cardiac implant, Appl. Phys. Lett. **101** (7), 073701 (2012).

[35] D. A. Iero, L. Crocco, and T. Isernia, On the role and choice of source polarization in time-reversal focusing of vector fields, IEEE Antennas Wirel. Propag. Lett. **15**, 214 (2015).